Airborne based spectroscopy of red and far-red sun-induced chlorophyll fluorescence: Implications for improved estimates of gross primary productivity

S. Wieneke [a,*], H. Ahrends [b], A. Damm [c], F. Pinto [d], A. Stadler [e], M. Rossini [f], U. Rascher [d]

[a] Hydrogeography and Climatology Research Group, University of Cologne, Zülpicherstrasse 45, 50674 Cologne, Germany
[b] Institute of Crop Science and Plant Breeding, University of Kiel, Hermann-Rodewald-Str. 9, 24118 Kiel, Germany
[c] Remote Sensing Laboratories, University of Zurich, Winterthurerstrasse 190, 8057 Zurich, Switzerland
[d] Institute of Bio- and Geosciences (IBG-2): Plant Sciences, Forschungszentrum Jülich GmbH, Leo-Brandt-Str., Jülich, Germany
[e] Institute of Crop Science and Resource Conservation, University of Bonn, Katzenburgweg 5, 53115 Bonn, Germany
[f] Remote Sensing of Environmental Dynamics Lab, DISAT, Università degli Studi Milano-Bicocca, Milan, Italy

ARTICLE INFO

ABSTRACT

Remote sensing (RS) approaches commonly applied to constrain estimates of gross primary production (GPP) employ greenness-based vegetation indices derived from surface reflectance data. Such approaches cannot capture dynamic changes of photosynthesis rates as caused by environmental stress. Further, applied vegetation indices are often affected by background reflectance or saturation effects. Sun. induced chlorophyll fluorescence (F) provides the most direct measure of photosynthesis and has been recently proposed as a new RS approach to improve estimates of GPP and tracing plant stress reactions. This work aims to provide further evidence on the complementary information content of F and its relation to changes in photosynthetic activity compared to traditional RS approaches. We use the airborne imaging spectrometer *HyPlant* to obtain several F products including red fluorescence (F_{687}), far-red fluorescence (F_{760}), F_{760} yield ($F_{760yield}$) and the ration between F_{687} and F_{760} (F_{ratio}). We calculate several vegetation indices indicative for vegetation greenness. We apply a recently proposed F-based semi-mechanistic approach to improve the forward modeling of GPP using F_{760} and compare this approach with a traditional one based on vegetation greenness and ground measurements of GPP derived from chamber measurements. In addition, we assess the sensitivity of $F_{760yield}$ and F_{ratio} for environmental stress. Our results show an improved predictive capability of GPP when using F_{760} compared to greenness-based vegetation indices. $F_{760yield}$ and F_{ratio} show a strong variability in time and between different crop types suffering from different levels of water shortage, indicating a strong sensitivity of F products for plant stress reactions. We conclude that the new RS approach of F provides complements to the set of commonly applies RS: The use of F_{760} improves constraining estimates of GPP while the ratio of red and far-red F shows large potential for tracking spatio-temporal plant adaptation in response to environmental stress conditions.

1. Introduction

Photosynthesis is a complex physiological ecosystem process that determines plant CO_2 uptake. On ecosystem scale photosynthesis is often referred as gross primary production (GPP). It is regulated by various biophysical processes and chemical reactions, which dynamically adapt to changing environmental conditions (Farquhar et al., 2001). As a consequence, spatial and temporal patterns of GPP are determined by environmental factors and the plant's ability to adapt to them.

Although accurate observations of temporal and spatial GPP patterns are important, making these observations at the landscape scale is still challenging. One possibility is to use eddy covariance (EC) flux towers, which measure the net carbon dioxide (CO_2) exchange of vegetated ecosystems with the atmosphere, and to partition the resulting fluxes into GPP and ecosystem respiration. EC flux towers, however, only represent small areas in pre-selected ecosystem (Drolet et al., 2008). Process modeling (Sitch et al., 2003) or combinations of in-situ EC observations and statistical modeling (Jung et al., 2011) provide estimates of GPP at across-spatial scales but are challenged by the complexity of natural systems and do not sufficiently account for actual photosynthetic rates. Recently, Schimel et al. (2015) even showed how model results are biased since their parameterization depends on

* Corresponding author.
E-mail address: swieneke@uni-koeln.de (S. Wieneke).

observations that are not spatially distributed according to carbon stocks.

Space- and airborne-based spectroscopy can be considered the only technology that measures important information about vegetation status and functions at broad scale, thus providing regional and global GPP information. Typically, vegetation indices (VIs) derived from optical measurements are employed in estimating GPP, under the assumption that physiological plant processes and the biochemical composition of vegetation canopies determine the optical properties of vegetation canopies (Hilker et al., 2008). The foundation of most remote sensing (RS) approaches used to estimate GPP is the resource balancing paradigm (Field et al., 1995), which hypothesizes that the plant's investment in the various resource-harvesting complexes is balanced and that plant growth can be sufficiently estimated by measuring only one growth-limiting factor. This idea – aligned to the measurement of light – is conceptualized in Monteith's light use efficiency (LUE) model (Monteith, 1972; Monteith and Moss, 1977); a model used in all RS-based GPP approaches (see Eq. 1):

$$GPP = PAR * fAPAR * LUE \qquad (1)$$

The model sets GPP in a proportional relationship with the incident of photosynthetically active radiation (PAR), the fraction of PAR absorbed by the vegetation (fAPAR), and the photosynthetic light use efficiency (LUE; defined as the amount of μmol CO_2 absorbed per μmol photons). The challenge in RS is to parameterize the three terms of Monteith's equation.

According to Hilker et al. (2008), fAPAR can be estimated through various methods, some of them based on its empirical non-linear relationship to VIs e.g., to the normalized difference vegetation index (NDVI). However, the saturation of VIs in dense canopies and their sensitivity to the background contributions of soil or non-photosynthetic vegetation components often lead to GPP being overestimated for sparse and less productive canopies and underestimated for dense and high productive canopies (Huete et al., 2002; Turner et al., 2003; Running et al., 2004; Xiao et al., 2008). Quantifying LUE is challenging and direct measurements are not yet possible. Besides unrealistically assuming a constant LUE, more sophisticated approaches adjust biome-specific potential LUE values by using meteorological variables derived from in-situ measurements and geo-statistical modeling (Jung et al., 2011; Running et al., 2004; Ryu et al., 2011; Xiao et al., 2004). Described approaches are based on vegetation greenness and do not show a direct mechanistic connection to actual photosynthesis, which is characterized by rapid and short-term adaptations to changing environmental conditions (e.g., fluctuating light, short term drought). Consequently, greenness-based approaches tend to be more related to potential than to actual photosynthetic rates (Meroni et al., 2009).

Recently, sun-induced chlorophyll fluorescence (F) was proposed as a means of overcoming these limitations when estimating GPP. Light energy absorbed by the plant is being channeled to three competitive pathways: (1) photosynthesis, (2) heat dissipation (non-photochemical quenching (NPQ)), and (3) F emission. Consequently, F is theoretically related to both APAR and LUE and opens up new perspectives for making GPP estimates more accurate.

Emitted F light has a well-defined spectral shape with two major peaks at 685 nm ($maxF_{<685>}$; red) and 740 nm ($maxF_{<740>}$; far-red) (Franck et al., 2002). The radiance signal received at an RS sensor comprises two radiance fluxes: sunlight reflected by the surface and the emitted F. The F radiation signal weakly adds to the reflected surface radiance (1–5% in the far-red), making the detection of F from RS data challenging. Analytical and technical developments nowadays allow F to be reliably measured using ground (Burkart et al., 2015; Cogliati et al., 2015; Damm et al., 2010a), airborne (Damm et al., 2010b, 2011, 2014; Rossini et al., 2015; Rascher et al., 2015), and satellite sensors (Frankenberg et al., 2014; Guanter et al., 2012; Joiner et al., 2011, 2012, 2013; Frankenberg et al., 2011a, 2011b; Frankenberg et al.,

2011a, 2011b; Frankenberg et al., 2012). These developments make it possible to study the mechanistic link between F and GPP in time and space (Damm et al., 2010a; Guanter et al., 2014; Zarco-Tejada et al., 2013; Rossini et al., 2015; Yang et al., 2015; Zhang et al., 2014).

The complexity of F-GPP relationships, recently discussed in Damm et al. (2015), requires further understanding and experimental evaluation of the robustness of this link as well potentially confounding factors (Porcar-Castell et al., 2014). Aim of this study is to elaborate on the mechanistic link between F and changes in photosynthetic activity as well on confounding factors. Maps of F_{760} and F_{687} (fluorescence at the wavelengths of 687 nm and 760 nm respectively) as well as several VIs were derived from the novel airborne image spectrometer *HyPlant* during three overflights around solar noon in August 2012 (Rascher et al., 2015). We use the semi-mechanistic approach by Guanter et al. (2014) to calculate GPP maps in high spatio-temporal resolution using resulting F_{760} maps. We compare F_{760} based GPP (GPP_{F760}) estimates with GPP based on common greenness-based approaches (GPP_{VI}) and validate them with ground measurements of GPP derived from parallel gas-exchange chamber measurements. Furthermore we analyzed the spatio-temporal changes of F products, particularly F_{687}, F_{760}, their ratio, and F_{yield}.

2. Material and methods

2.1. Study area

The study area close to the village of Selhausen (50.864 N, 6.452 E, altitude 103 m above sea level) is located in the Rur catchment in the central western part of North Rhine-Westphalia, Germany (Fig. 1 A&B). The Rur catchment is an intensive study area of the Transregional Collaborative Research Centre 32 (TR32, http://tr32new.uni-koeln.de/), founded by the German Research Foundation. Within the study area, one sugar beet field was selected as an experimental site for ground measurements. The experimental site covers 1.4 ha (200 m × 70 m) with a gentle slope of 4° in east-west direction. The upper part of the field is more gravelly than the lower part, resulting in a lower water-holding capacity in that area (Rudolph et al., 2015; Stadler et al., 2015). The climate is characterized by an annual mean temperature of 11 °C and an annual mean precipitation of around 700 mm/year (Lanuv, 2014). The region is dominated by agriculture. The dominant crop type is sugar beet followed by maize, rapeseed, and potatoes.

This study focuses on sugar beet, which grew in 2012 from March (day of year (DOY): 87) to September (DOY: 254). Ground measurements were carried out in sugar beet field G (Fig. 1C) with fully developed leaves and a fractional cover of 90% (BBCH-Code: 39 – the Biologische Bundesanstalt, Bundessortenamt und CHemische Industrie (BBCH) code describes the phenological status of a plant. BBCH-Code: 39 indicate that the Rosette growth is completed and that leaves cover 90% of the ground). Imaging spectroscopy data were acquired with the *HyPlant* sensor on August 23, 2012 (DOY: 236). The observation took place under clear sky conditions. A rain event with a precipitation sum of 0.12 mm was recorded one day before the airborne data acquisition, and the maximum air temperature was 23 °C. Sunrise was at 4:32 a.m., solar noon at 11:35 a.m. and sunset at 6:36 p.m. UTC (Coordinated Universal Time).

2.2. Ground measurements

2.2.1. Field spectroscopy to estimate F_{760}, $APAR_{MSS}$ and $F_{760yield}$

During the flight campaign, the custom-made measurement setup Manual Spectrometric System (MSS) was used to continuously measure irradiance and surface-leaving radiance to eventually derive F emissions at 760 nm (F_{760}) as well as the absorbed photosynthetic active radiation ($APAR_{MSS}$). The spectrometer system was designed for high-temporal frequency sampling of radiometric measurements. Briefly, top of canopy radiances were measured using two portable spectrometers
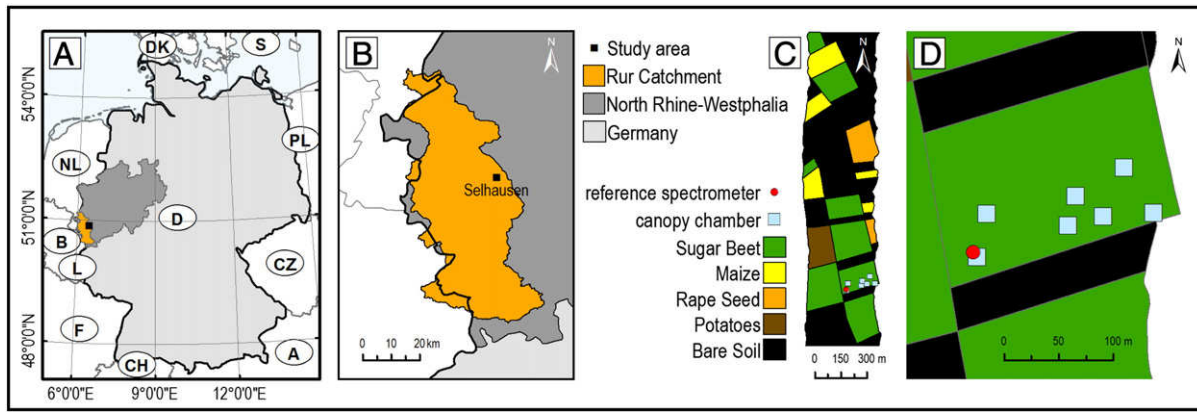
Fig. 1. Study area location within Germany (A), the catchment area of the river Rur (B), land use classification of the flight line (C), position of the MSS reference spectrometer and the net ecosystem exchange canopy chambers (D).

(HR4000, OceanOptics, USA) characterized by different spectral resolutions. The first instrument covered the visible and near-infrared range (400 nm to 1000 nm) with a full width at half maximum (FWHM) of 1 nm, facilitating the computation of different VIs. The second instrument covered a restricted spectral range (700 nm to 800 nm) with a finer spectral resolution (FWHM = 0.1 nm) and was specifically intended for F_{760} measurements in the oxygen absorption band O2-A. Both spectrometers were housed in a Peltier thermally regulated box (model NT-16, Magapor, Zaragoza, Spain), keeping the internal temperature at 25 °C to reduce dark current drifts. Both spectrometers were spectrally and radiometrically calibrated with known standards (CAL-2000 mercury argon lamp and LS-1-CAL calibrated tungsten halogen lamp, OceanOptics, USA). The instrument's fiber optics were mounted on a horizontal rotating arm to observe alternately the canopy and a calibrated white reference panel (Labsphere, Inc., USA) and thus to measure surface irradiance. The MSS was installed on a fixed position (Fig. 1D) but the 1.5 m radial-arm was sequentially (ca. 1–3 min) placed over three positions and observations were averaged to cover potential field heterogeneity. Measurements started at 8:35 a.m. and finished at 4:10 p.m. UTC.

F_{760} emissions were retrieved using the spectral fitting method (SFM, (Meroni et al., 2010)), assuming a linear variation of reflectance and fluorescence in the O2-A absorption band region (759.0 nm to 767.7 nm). Resulting F values are hereafter named $F_{760,MSS}$. Detailed technical information about the F retrieval approach is reported in (Rossini et al., 2010)). $APAR_{MSS}$ was derived from measured radiances as the difference between incident and reflected radiance, integrated over the spectral region from 400 nm to 700 nm (Damm et al., 2010a). F_{yield} is the fluorescence use efficiency, indicating the fraction of photons that are re-emitted from the absorbed photons. We calculated $F_{760yield}$ from MSS measurements as:

$$F_{760yieldMSS} = \frac{F_{760MSS}}{APAR_{MSS}} \quad (2)$$

2.2.2. Canopy gas-exchange chamber and leaf area index measurements

We permanently installed seven connector frames at different positions within a sugar beet field (Fig. 1D). The chamber comprised a 50 cm height adapter and a 30 cm height chamber top. The chamber top was equipped with a LI-COR 6400 XT IRGA (LI-COR, Lincoln Nebraska, USA) gas analyzer and was moved between the connector frames during the flight campaign to measure NEE_{CC} (μmol CO_2 m^{-2} s^{-1}) and PAR_{CC} (μmol m^{-2} s^{-1}). Detailed technical information about the measurement setup can be found in Langensiepen et al. (2012). Soil respiration ($R_{soil,CC}$, μmol CO_2 m^{-2} s^{-1}) was measured using a LI-8100 (LI-COR, Lincoln Nebraska, USA) soil gas analyzer within the connector

frames. The measurements started around 8:10 a.m. and ended at 3:00 p.m. UTC, resulting in five measurements per chamber position. The partitioning of NEE_{CC} into GPP_{CC} and respiration fluxes can be expressed as:

$$GPP_{CC} = -NEE_{CC} + (R_{soil,CC} + R_{plant,CC}) \quad (3)$$

Since no dark chamber measurements where available, $R_{plant,CC}$ could not be obtained directly from the chamber measurements. To estimate $R_{plant,CC}$ we used measurements of an nearby EC tower positioned in a sugar beet field at the same growing stage. Based on the assumption that field mean $R_{CC,soil}$ and $R_{EC,soil}$ are not significantly different, $R_{plant,CC}$ was calculated as:

$$R_{EC,plant} \approx R_{EC,ecosystem} - R_{CC,soil} \quad (4)$$

and:

$$R_{CC,plant} \approx \frac{R_{EC,plant}}{NEE_{EC}} * NEE_{CC} \quad (5)$$

For the flux partitioning of the NEE_{EC}, we used the online processing tool based on (Reichstein et al., 2005). Because the measurement intervals were irregular, observation times were harmonized by linearly interpolating chamber data. To ensure that the chamber measurements were not significantly distorted due to microclimate alteration within the chamber, we correlated GPP_{CC} with the destructively-measured leaf area index (LAI). The LAI measurements were conducted on the day of flyovers with a leaf area meter LI-3100C (LI-COR Bioscience, Lincoln, Nebraska) at the position of the canopy chambers (Fig. 1D). The significant positive relationship ($R^2 = 0.84$) between derived GPP_{CC} and measured LAI indicates that the chamber measurements captured the infield variability of GPP well. To account for measurement and interpolation errors due to the lack of $R_{CC,plant}$, we assume an uncertainty of 10% (Graf et al., 2013; Wang et al., 2013).

APAR needs to be known to calculate LUE_{CC} from chamber measurements. PAR was measured by the individual canopy chambers and fAPAR was modeled using the radiative transfer model SCOPE version 1.51 (van der Tol et al., 2009), parameterized with in-situ measured LAI and half-hourly atmospheric data obtained from a nearby meteorological station. We applied an average chlorophyll a and b concentration of 80 mg cm^{-2} and a maximum carboxylation rate (Vcmax) of 80 μmol m^{-2} s^{-1}. The Ball Berry stomatal conductance parameter was set to ten and the vegetation height was set to 0.6 m. A spherical leaf distribution of the sugar beet plants was assumed. Further details on the SCOPE model can be found in van der Tol et al., (2009).

2.3. Airborne (HyPlant) measurements

Airborne images were acquired on 23rd August 2012 using the imaging spectrometer *HyPlant* (Specim, Oulo, Finland). *HyPlant*, which has been operated since 2012 by the research center Jülich, was developed within the framework of ESA's Fluorescence Explorer (FLEX) mission Phase A activities and is an airborne demonstrator for the FLEX satellite mission. It was specifically designed to monitor functional vegetation information, including emitted F and other important plant functional traits. The instrument is a push-broom imager consisting of two modules measuring surface radiance in the spectral ranges from 380 nm to 2500 nm (DUAL module) and from 670 nm to 780 nm (FLUO module). The high resolution FLUO module covers the red and far-red region of the electromagnetic spectrum with high spectral resolution (FWHM of 0.25 nm). This allows the retrieval of emitted F signals in two atmospheric oxygen bands, O_2-A (760 nm; F_{760}) and O_2-B (687 nm; F_{687}). The good performance of *HyPlant* enables for the first time F_{760} and F_{687} to be measured in high spatial resolution at field and ecosystem scale (Rossini et al., 2015). Technical details, sensor calibration, image preprocessing, and validation are described in Rascher et al. (2015).

In this study, we use F_{760} and F_{687} (cf., Section 0) and VIs products (cf. Section 2.4.1) derived from the *HyPlant* sensor. Flight lines were recorded at 600 m above ground, with a spatial resolution of 1 m.

2.3.1. F_{760} and F_{687} retrieval

Emitted chlorophyll fluorescence adds to the radiation flux reflected by a vegetation canopy. Quantifying F requires analytically disentangling both fluxes, usually by using contrasting wavelength regions in the vicinity of strong atmospheric or solar absorption features (Meroni et al., 2010). Assuming Lambertian surface reflectance (R), measured at-sensor radiance signals of a vegetation target (L) inside (i) and outside (o) a certain absorption band can be expressed as:

$$L_j = \frac{E_j^0 \cos\theta_{il}}{\pi}\left[\rho_{so}^j + \frac{\left(\tau_{ss}^j\tau_{oo}^j + \tau_{sd}^j\tau_{oo}^j + \tau_{ss}^j\tau_{do}^j + \tau_{sd}^j\tau_{do}^j\right)R_j}{1-R_j\rho_{dd}^j}\right] + \frac{F_j\left(\tau_{oo}^j + \tau_{do}^j\right)}{1-R_j\rho_{dd}^j}, j\in\{i,o\} \tag{6}$$

where E_j^0 is the top-of-atmosphere irradiance including diffuse and direct irradiance components, θ_{il} is the illumination zenith angle, ρ_{so} is the path scattered radiance, τ_{ss} is the direct transmittance for sunlight, τ_{oo} is the direct transmittance in view direction, τ_{sd} is the diffuse transmittance of the atmosphere for sunlight, τ_{do} is the hemispherical-directional transmittance in view direction, and ρ_{dd} is the spherical albedo.

When retrieving F from airborne data, only L_j is known and the various atmospheric transmittance functions, E, ρ_{so}, and ρ_{dd}, must be approximated using, for example, atmospheric radiative transfer models such as MODTRAN-5 (Berk et al., 2005) and the MODTRAN-interrogation technique introduced by Verhoef and Bach (Verhoef and Bach, 2003, 2007). The system of Eq. (6) then contains four unknowns: F_i, F_o, R_i, and R_o, which are spectral reflectance and fluorescence values, inside and outside of the absorption bands.

In this study, we retrieved F_{687} and F_{760} using the iFLD method (Alonso et al., 2008). The iFLD method is a modification of the original Fraunhofer Line Depth (FLD) approach (Plascyk and Gabriel, 1975) and allows relating R and F inside and outside of both absorption bands using polynomial functions. F at the respective wavelengths was accordingly calculated as:

$$F = \frac{B\left[\dfrac{X_i\left(E_o + X_o\rho_{dd}^o\right) - AX_o\left(E_i + X_i\rho_{dd}^i\right)}{B\left(E_o + X_o\rho_{dd}^o\right) - A\left(E_i + X_i\rho_{dd}^i\right)}\right]}{\tau_{oo}^i + \tau_{do}^i} \tag{7}$$

with

$$X_j = \left(L_j - \frac{E_j^o \cos\theta_{il}}{\pi}\rho_{so}^j\right), \qquad j = i, o \tag{8}$$

$$E_j = \frac{E_j^o \cos\theta_{il}}{\pi}\left(\tau_{ss}^j\tau_{oo}^j + \tau_{sd}^j\tau_{oo}^j + \tau_{ss}^j\tau_{do}^j + \tau_{sd}^j\tau_{do}^j\right), \quad j = i, o \tag{9}$$

$$\left.\begin{array}{c} R_i = AR_o \\ F_i\left(\tau_{oo}^i + \tau_{do}^i\right) = BF_o\left(\tau_{oo}^o + \tau_{do}^o\right) \end{array}\right\} \tag{10}$$

X_j equals the at-sensor radiance (reflected plus emitted radiation) without path radiance contribution and E_j expresses surface irradiance as measured at sensor level. B is an empirical correction factor that relates F_i and F_o and was set to a value of 1.0 and 0.8 for F_{687} and F_{760}, justified by simulations and experiments (Alonso et al., 2008; Rascher et al., 2009). A is the factor relating R_i, and R_o and was derived from a polynomial fitting approach using reflectance values of the left and right side of the respective absorption bands.

The MODTRAN-5 model was parameterized using measurements taken under stable atmospheric conditions and estimating all atmospheric functions for a flat surface assuming a standard atmosphere. Solar zenith, solar azimuth, ground elevation, and sensor elevation were adjusted to the measurement times. However, we applied a semi-empirical correction called "transmittance correction" for each scan line across track to compensate for slight inaccuracies in the atmospheric modeling and instrumental errors (e.g., spectral shift residuals, vignetting effects), which can cause uncertainties in retrieved F_{687} and F_{760} signals (Damm et al., 2011). This technique uses reference surfaces free of any F emission (e.g., bare soil) and retrieves a correction factor that allows adjusting the upward transmittance term inside the absorption feature τ_{oo}^i (see Damm et al. (2014) for details on this method).

Variations in absolute F values can be expected, since F_{760} and $F_{760,MSS}$ were retrieved with different methods (SFM for MSS and iFLD for *HyPlant*) and from different sensors that have different sensor dependencies on the point spread function (c.f. Damm et al., 2011). The comparison of *HyPlant*-based F_{760} with $F_{760,MSS}$ shows best agreements for the 11:50 a.m. UTC overflight with an 5.7% overestimation ($F_{760,MSS} = 2.04\,\text{mW}\,\text{m}^{-2}\,\text{nm}^{-1}\,\text{sr}^{-1}$, $F_{760} = 2.13\,\text{mW}\,\text{m}^{-2}\,\text{nm}^{-1}\,\text{sr}^{-1}$). The 9:56 a.m. and the 2:05 p.m. overflights underestimate F_{760} by 4.4% ($F_{760,MSS} = 1.75\,\text{mW}\,\text{m}^{-2}\,\text{nm}^{-1}\,\text{sr}^{-1}$, $F_{760} = 1.65\,\text{mW}\,\text{m}^{-2}\,\text{nm}^{-1}\,\text{sr}^{-1}$) and 31.3% ($F_{760,MSS} = 1.66\,\text{mW}\,\text{m}^{-2}\,\text{nm}^{-1}\,\text{sr}^{-1}$, $F_{760} = 1.14\,\text{mW}\,\text{m}^{-2}\,\text{nm}^{-1}\,\text{sr}^{-1}$), respectively. A linear scaling approach was applied to compensate for the underestimation of *HyPlant*-based F_{760} values.

2.3.2. Calculation of vegetation indices

We tested five commonly applied VIs sensitive to different properties of vegetation canopies. As biomass sensitive indices, we evaluated the normalized different VIs, NDVI, (Rouse et al., 1973), and the enhanced vegetation index, EVI, (Huete et al., 2002). Both, the transformed chlorophyll *a*bsorption in reflectance index, TCARI, (Haboudane et al., 2002) and the modified chlorophyll absorption ratio index, MCARI2, (Haboudane et al., 2004) were tested as sensitive indices for green biomass. We also investigated the performance of the photochemical reflectance index, PRI, (Gamon et al., 1992), sensitive to pigment changes related to the xanthophyll cycle and frequently employed as proxy for LUE. The equations for all listed indices can be found in Table 1.

2.3.3. Calculation of fluorescence yield

In absence of $F_{687yield}$ ground observations, spatial maps of $F_{760yield}$ only were calculated from *HyPlant*-derived F_{760} maps as:

$$F_{760yield} = \frac{F_{760}}{PAR_{CC} * fAPAR_{VI}} \tag{11}$$

where PAR_{CC} corresponds to the mean of all canopy chambers (cf.,

Table 1
Equations for examined spectral vegetation indices.

Equation	Reference
$NDVI = \frac{R_{800} - R_{670}}{R_{800} + R_{670}}$	Rouse et al (1973)
$EVI = 2.5 * \frac{R_{800} - R_{670}}{R_{800} + 6 * R_{670} - 7.5 * R_{400} + 1}$	Huete et al. (2002)
$PRI = \frac{R_{570} - R_{531}}{R_{570} + R_{531}}$	Gamon et al. 1(992)
$TCARI = 3 * [(R_{700} - R_{670}) - 0.2 * (R_{700} - R_{550}) * (\frac{R_{700}}{R_{670}})]$	Haboudane et al. (2002)
$MCARI2 = \frac{1.5 * (2.5 * (R_{800} - R_{670}) - 1.3 * (R_{800} - R_{550}))}{\sqrt{2 * (R_{800} + 1)^2 - (6 * R_{800} - 5 * \sqrt{R_{670}}) - 0.5}}$	Haboudane et al. (2004)

Section 2.2.2), and spatial maps of $fAPAR_{VI}$ were derived from VIs as:

$$fAPAR_{VI} = k * VI \qquad (12)$$

with k estimated from the relationship between in-field modeled $fAPAR_{CC}$ (cf., Section 2.2.2) and all *HyPlant* VIs for each individual flight line.

2.4. Spatio-temporal estimation of sugar beet GPP

2.4.1. GPP estimation based on VIs

We calculated GPP maps for the three overflights using Monteith's LUE approach (Monteith, 1972) and approximated fAPAR as a function of different VIs. The resulting GPP_{VI} can be expressed as:

$$GPP_{VI} = PAR_{CC} * fAPAR_{VI} * LUE_{CC} \qquad (13)$$

The used diurnal cycle of PAR_{CC} corresponds to the mean of seven canopy chamber measurements. Actual LUE_{CC} for sugar beet was calculated for each overflight time window as:

$$LUE_{CC} = \frac{GPP_{CC}}{APAR_{CC}} \qquad (14)$$

where GPP_{CC} corresponds to the mean of the seven canopy chambers and $APAR_{CC}$ to the averaged model results (cf., Section 2.2.2).

2.4.2. GPP estimation based on F_{760}

Since ground-based F_{687} measurements were not available, only *HyPlant*-based F_{760} measurements were used to calculate spatial maps of GPP (GPP_{F760}) using an approach derived from (Guanter et al., 2014). In analogy to Eq. (1), F is described as:

$$F = PAR * fAPAR * F_{yield} \qquad (15)$$

If Eqs. (1) and (15) are re-arranged and combined, GPP can be finally calculated as:

$$GPP = F * \frac{LUE}{F_{yield}} \qquad (16)$$

To calculate maps of GPP_{F760}, we replaced F with *HyPlant*-based F_{760}, F_{yield} with $F_{760yield}$, and LUE with LUE_{CC}.

2.5. Model validation and uncertainty

We calculated the mean of GPP_{VI} and GPP_{F760} within a three meter buffer around the canopy chamber positions to minimize potential errors of the canopy chamber global positioning system and errors related to the point spread function of *HyPlant*. Further, we estimated the random error of all GPP_{VI} and GPP_{F760} by defining a homogenous training area within the maps. Additionally, we considered the systematic error in the F_{760} retrieval method (Damm et al., 2011) and the random error in the F_{760} ground measurements.

3. Results

3.1. Diurnal dynamics of F_{760}, F_{687}, their ratio and LUE

HyPlant's first fluorescence maps demonstrating diurnal changes in both fluorescence peaks are shown in Fig. 2. Maps of F_{760} and F_{687} show the highest fluorescence values during solar noon and lower values in the morning and afternoon. The highest values of F_{760} and F_{687} were measured within the sugar beet fields. The F_{760} maps show spatial patterns similar to the reflectance-based EVI, with a gradient of F_{760} values from the field borders to the field center. The F_{687} maps are noisier and for most fields lower (around twofold) than average F_{760} values. In contrast, during solar noon F_{687} for sugar beet field B and rapeseed field C show higher values than F_{760}. A fundamental difference can be seen in all maize fields, where F_{760} and F_{687} values are very low and stable over the day. In general, sugar beet field B shows higher heterogeneity than sugar beet fields D to H. (Fig. 2). Fig. 3 shows the ratio between F_{687} and F_{760} (F_{ratio}). Highest values of F_{ratio} are found in parts of sugar beet field B where plants undergo a severe drought stress due to gravely soil. All rapeseed fields, which are in early growing stage, show increased F_{ratio} values. The F_{ratio} in sugar beet field B is highest during noon, while F_{ratio} in the rapeseed fields reaches maximum values in the afternoon. Sugar beet fields D, E, F, G and H show little change in the F_{ratio} except for areas with low EVI where plants again suffer from severe drought stress (eastern field boarder of D, E and G, Fig. 3).

Diurnal dynamics were analyzed in more detail using the ground-based measurements. Field averaged $APAR_{CC}$, used for the LUE_{CC} calculation, increased to a maximum of 1300 µmol m^{-2} s^{-1} at solar noon. The field average GPP_{CC} sharply increased from sunrise to a maximum CO_2 uptake of 35 µmol CO_2 m^{-2} s^{-1} at 9.20 a.m. UTC. Afterwards the uptake slowly decreased until 3.00 p.m. UTC, when the measurements stopped (Fig. 4A). During the morning hours, we observed a decrease of field averaged LUE_{CC} from 0.037 to a minimum of 0.024 after solar noon and a subsequent increase to 0.029 until the end of measurements at 3 p.m. (Fig. 4C).

MSS measurements started at 8:35 a.m. with $APAR_{MSS}$ values of 255 Wm^{-2} and F_{760} values of 1.48 mW m^{-2} sr^{-1} nm^{-1}. $APAR_{MSS}$ and F_{760} followed a typical diurnal cycle for clear sky conditions, albeit with F_{760} fluctuating more strongly. The maxima of $APAR_{MSS}$ and F_{760} were reached around 11 a.m. with 350 W m^{-2} and 2.4 mW m^{-2} sr^{-1} nm^{-1}. Both values decreased ($APAR_{MSS}$ = 220 W m^{-2} s^{-1} and F_{760} = 1.3 mW m^{-2} sr^{-1} nm^{-1}) until 3:00 p.m. (Fig. 4B). To reduce the noise of the F_{760} signal, we calculated a moving average for the $F_{760yield,MSS}$. From 8:35 a.m. to 12:40 p.m., $F_{760yield,MSS}$ showed a steady decrease from 0.0066 to 0.0056. Afterwards, it steadily increased to 0.0070 at 3:00 p.m. (Fig. 4C).

The resulting relationship between LUE_{CC} and $F_{760yield,MSS}$ changed over the measurement day resulting in a relative low coefficient of
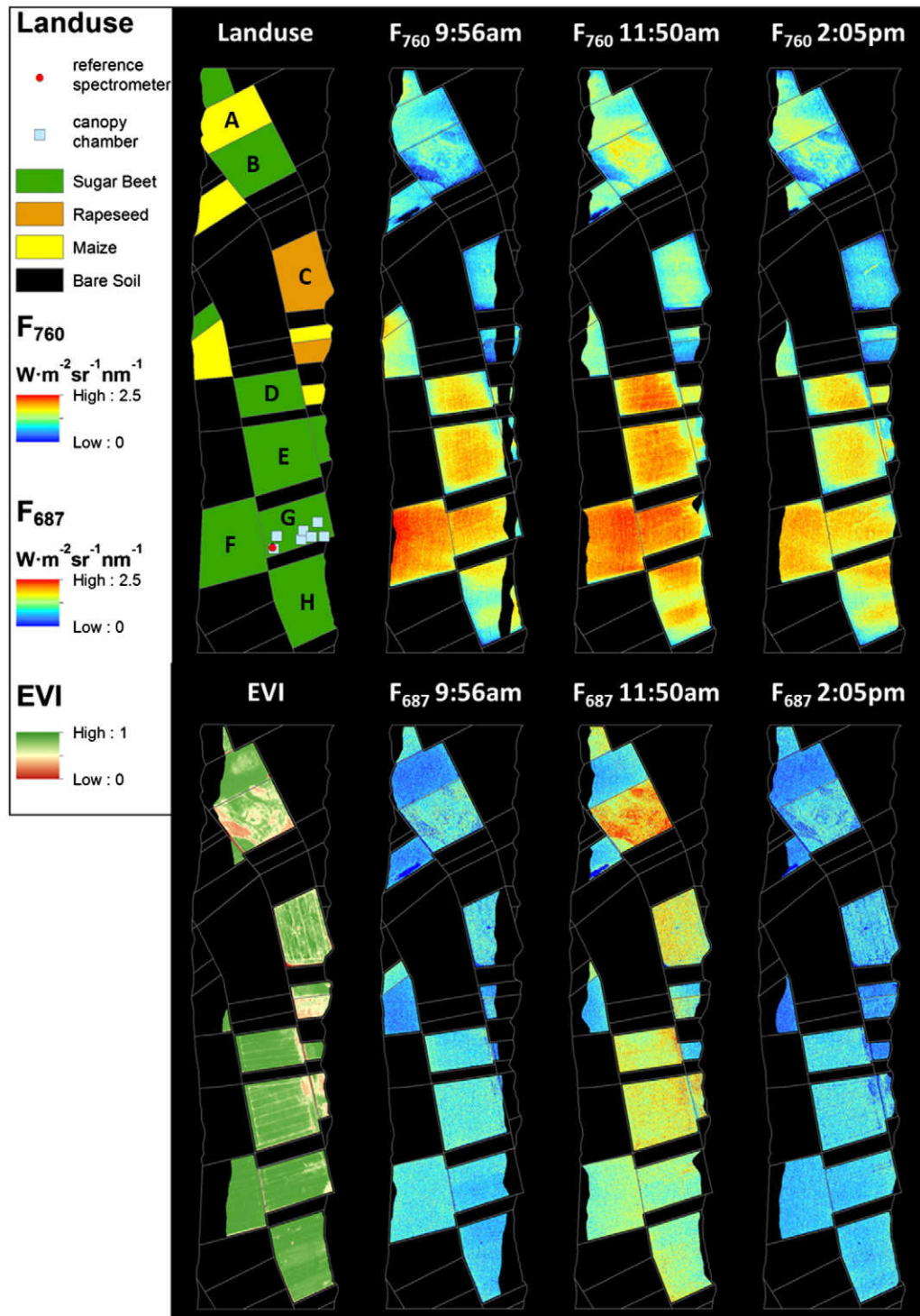
Fig. 2. Maps of fluorescence at 760 nm (F_{760}) and 687 nm (F_{687}) recorded at 9:56 a.m., 11:50 a.m. and 2:05 p.m. Only the F_{760} maps were validated with ground measurements. Upper left map shows the land use of the flight line, the position of the reference spectrometer (MSS) and the location of the canopy chambers used to derive GPP_{CC}. Lower left map shows the enhanced vegetation index (EVI).

determination ($R^2 = 0.17$). From 8:35 a.m. to solar noon, the ratio between LUE_{CC} and $F_{760yield,MSS}$ showed a strong decrease, followed by a more or less constant relationship by the end of measurements (Fig. 4D). In Fig. 5, we evaluate the relationship between LUE_{CC} and the averaged $F_{760yield,MSS}$ separately for data acquired before and after LUE_{CC} and $F_{760yield,MSS}$ are lowest (1 h after solar noon) . From morning to 12:45 p.m. the relationship between LUE_{CC} and $F_{760yield,MSS}$ shows an exponential decrease with an R^2 of 0.8. After 12:45 p.m. $F_{760yield,MSS}$ values are characterized by a wider range than the LUE_{CC} values, leading

to a steep slope coefficient of the linear regression fit and a higher coefficient of determination ($R^2 = 0.95$).

3.2. GPP estimation of sugar beet fields

We used five different VIs to calculate GPP estimates from the remote sensing data (GPP_{VI}, cf., Section 2.4.1). Results showed a high agreement between the GPP_{CC} values at medium levels of ~25–35 μmol CO_2 m^{-2} s^{-1}. However, for the lower and the upper data
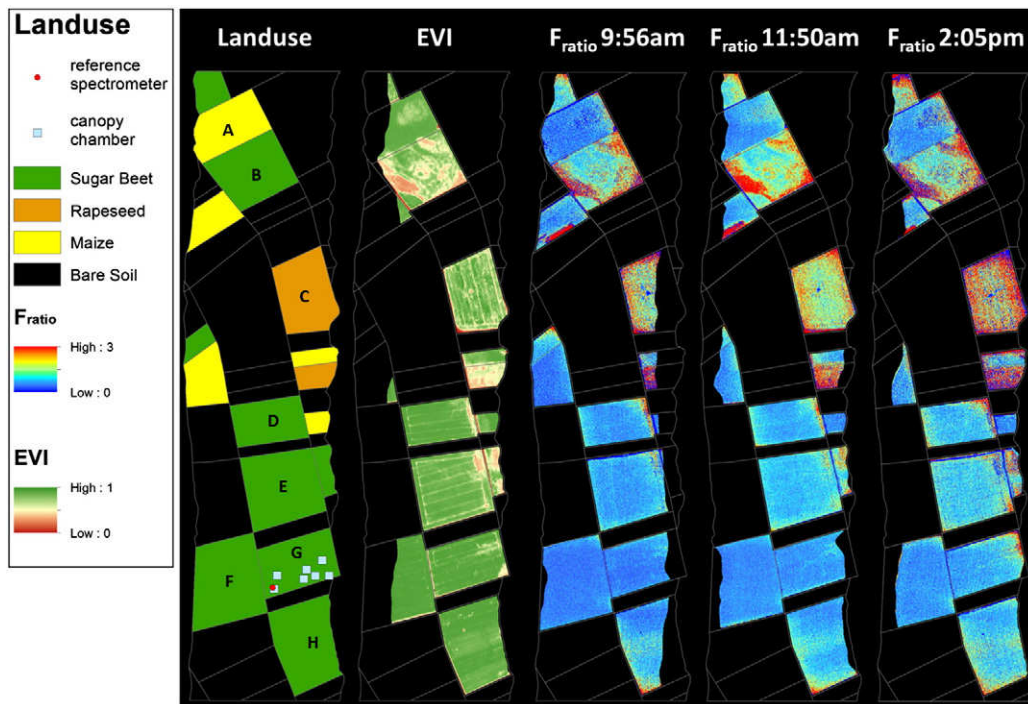
Fig. 3. Maps of F_{687} to F_{760} ratio (F_{ratio}) calculated for 9:56 a.m., 11:50 a.m. and 2:05 p.m. Left map shows the land use of the flight line, the position of the reference spectrometer (MSS) and the location of the canopy chambers used to derive GPP_{CC}. The map second from the left shows the enhanced vegetation index (EVI).

range, GPP_{VI}, calculations tend to over- or underestimate GPP. Highest agreement was found for the GPP_{EVI}. The relationship is significantly higher ($R^2 = 0.82$), the error lower (RMSE = 6.26 μmol CO_2 $m^{-2} s^{-1}$), and the slope closer to 1 (0.48) compared to all other GPP_{VI} estimations (Table 2). In a second step we calculated GPP using F760 (GPP_{F760}). The relationship of GPP_{CC} with GPP_{F760} ($R^2 = 0.87$) shown in Fig. 6 is higher than the relation with GPP_{EVI} ($R^2 = 0.82$). However, both methods underestimate GPP_{CC} ($GPP_{F760} = -5.9\%$ and $GPP_{EVI} = -3.7\%$) and show difficulties in representing the lower and the upper range of GPP_{CC} values. In summary, the considerably higher slope of the linear regression fit (cf. Fig. 6) calculated for the GPP_{F760} model (0.65) as compared to the GPP_{EVI} model (0.48) indicates that the F760 based approach is more suitable to capture low values of GPP. The root mean square error (RMSE) decreases from 5.26 μmol CO_2 $m^{-2} s^{-1}$ for the LUE model to 4.34 μmol CO_2 $m^{-2} s^{-1}$ for the GPP_{F760} model. The uncertainty range estimated for each sample point is, especially at high GPP_{CC} values, significantly higher for the estimated GPP_{F760} than for the GPP_{EVI}.

GPP_{EVI} and GPP_{760} maps (Fig. 7) indicate that highest productivity levels are reached before solar noon and lowest values can be observed in the afternoon. For homogenous fields with high plant coverage like D, F and G we see similar spatial patterns in the GPP_{EVI} and GPP_{F760} maps. Contrastingly, heterogeneous fields with areas of lower plant density (E, H and especially B) demonstrate the differences between GPP_{EVI} and GPP_{F760}. While field B and H have lower values in the GPP_{760} maps, we recognize higher values of GPP_{760} in field E compared with the GPP_{EVI} values. In general GPP_{EVI} maps indicate a more homogenous productivity level within the fields and are more sharply contoured compared with GPP_{F760} (e.g., tractor tracks are clearly visible in fields D, E, and G).

3.3. Spatio-temporal patterns of $fAPAR_{EVI}$ and $F_{760yield}$

$FAPAR_{EVI}$ and $F_{760yield}$ characterize the spatial patterns of the reflectance and fluorescence based models, respectively. We therefore compared these two parameters regarding their spatio-temporal changes during the measurement day. In general we detect lowest $F_{760yield}$

values for rapeseed field C and maize field A and highest values for sugar beet field D, E, F and G. $F_{760yield}$ increases from 9:56 a.m. to 11:50 a.m. within all agricultural fields (Fig. 8). Especially for field B, we observe a strong increase of $F_{760yield}$ during morning hours and, interestingly, the formation of a distinctive diurnal course with maximum values during solar noon and a decrease towards the afternoon. In contrast $F_{760yield}$ in the maize field (A in Fig. 8) constantly increased throughout the day and maximum values were measured in the afternoon.

The probability density functions (PDFs) of Fig. 9 illustrate the changes in fAPAR and $F_{760yield}$ that occur in the course of one day. Over the day, $fAPAR_{EVI}$ changes only slightly. The distribution of $F_{760yield}$ values, on the contrary, changes depending on overflight time and land use. For the more homogeneous sugar beet fields D to H, $F_{760yield}$ constantly increases over the day (Fig. 9B), while $F_{760yield}$ of the heterogeneous sugar beet field B decreases in the 2:05 p.m. overflight (Fig. 9D). Maize field A shows a constant increase of $F_{760yield}$ over the day with a proportionally stronger increase in the 2:05 p.m. overflight (Fig. 9F). During the first two overflights, rapeseed field C showed an increase in $F_{760yield}$ and a decrease for the 2:05 p.m. overflight. Overall the sugar beet fields start and end with higher $F_{760yield}$ values than the maize and rapeseed fields in the morning and the afternoon.

4. Discussion

4.1. Reliability of retrieved F_{760} and F_{687} maps

HyPlant's FLUO module allows, for the first time, simultaneous retrievals of F_{760} and F_{687} in validated physical units with high spatial resolution (cf., Section 3.1 and Rascher et al. (2015)). Both, F_{760} and F_{687} maps appear noisy compared to the maps of calculated VIs (Fig. 2). These effects are caused by a combination of the lower signal to noise ratio (F emissions are a small radiation flux of the signal eventually measured at a remote sensor) and the detector sensitivity (the high spectral and spatial resolution reduces the energy actually measured at the detector array). However, apparent noise effects do not limit the
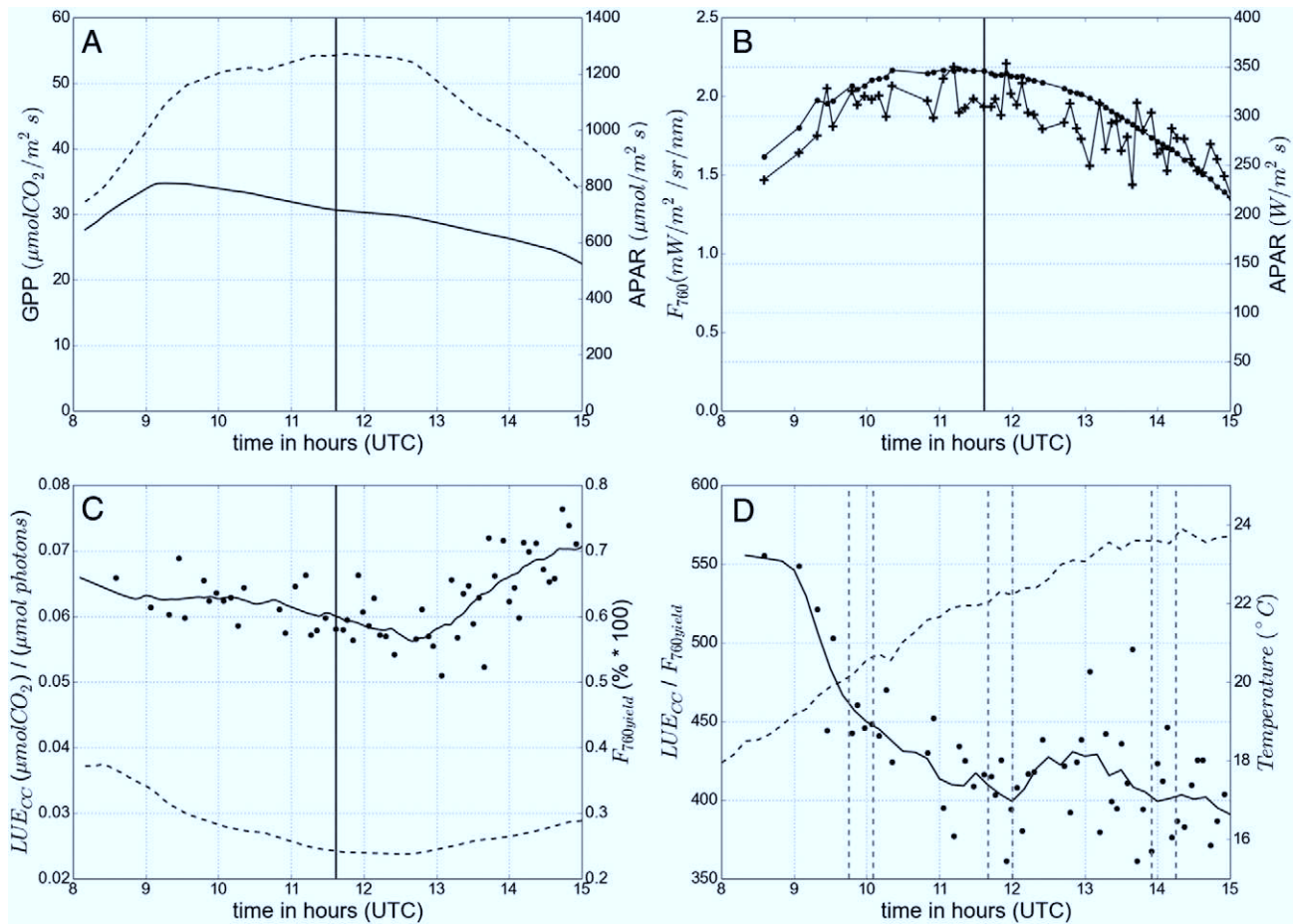
Fig. 4. Interpolated diurnal cycle of gross primary production (GPP; solid line) and absorbed photosynthetic active radiation (APAR; dashed line) averaged over seven net ecosystem exchange (NEE) chambers within a sugar beet field. Vertical line marks local solar noon (A). Diurnal sun-induced chlorophyll fluorescence (F_{760}; crosses) and APAR (dots) measured by Manual Spectrometric System (MSS). Vertical line marks local solar noon (B). Interpolated diurnal light use efficiency (LUE_{CC}; dashed line) derived from canopy chambers, $F_{760yield}$ (points) and moving average of $F_{760yield}$ (solid line) derived from MSS. Vertical line marks local solar noon (C). Diurnal relationship of LUE_{CC} to $F_{760yield}$ (points), moving averaged (solid line), diurnal course of temperature (dashed horizontal line) and flight windows (dashed vertical lines) (D).

interpretation of our F retrievals and can be further compensated by applying a spatial-spectral binning. We observed gradients in F_{760} and derived data products (i.e., GPP_{760}) from the border to the center of the fields. These gradients are partly caused by a sensor effect (i.e., a point spread function non-uniformity) which was solved by a hardware change in 2014 and thus will not be present in more recent data sets. This effect, however, does not impact our results since we deliberately analyzed measurements from the homogeneous field centers. We show some of the first maps of F_{687}, providing interesting insights into the information content of F. The higher variability of F_{687} to F_{760} was also documented by Rossini et al. (2015) over a grassland site and is most likely caused by the higher retrieval noise associated with the narrow O_2B absorption band.

4.2. Sensitivity of greenness based VI for plant functional changes

Results show that the EVI, which is sensitive to the canopy structure, performs best as a proxy for spatial variability of fAPAR in the LUE model (Table 2). Since the EVI was designed to be less sensitive to saturation
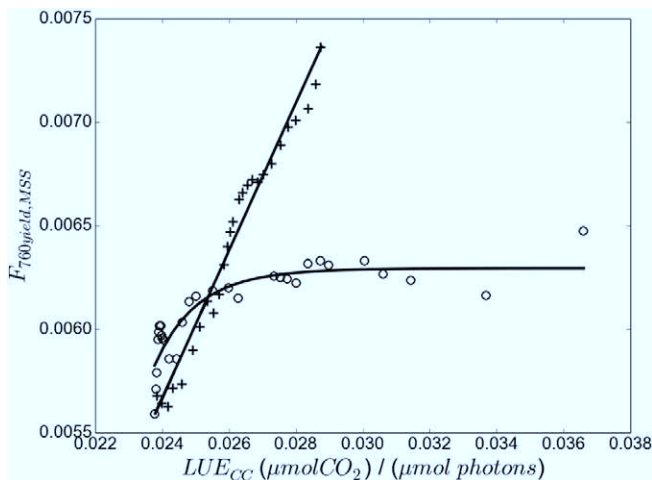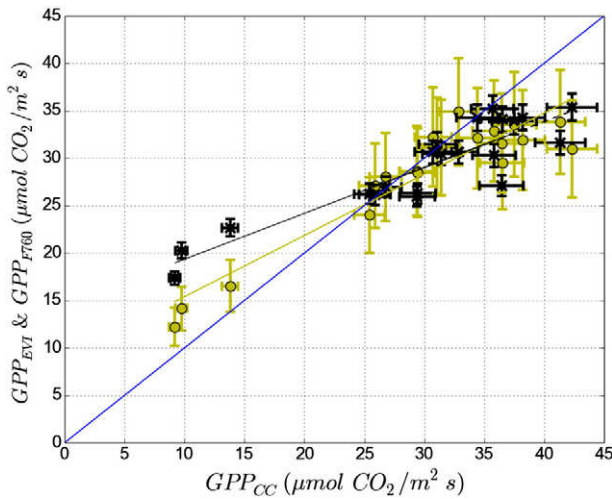

Fig. 5. Relationship of LUE_{CC} estimated from canopy gas-exchange chamber measurements and averaged $F_{760yield}$ from MSS fluorescence ground measurements. Points symbolize measurements until 12:45 p.m. UTC, crosses symbolize measurements from 12:45 p.m. UTC to 3:00 p.m. UTC. The lines show the respective slope of the relationship. The coefficient of determination (R^2) for before noon- and after 12:45 p.m. UTC are 0.80 and 0.95 respectively.

Table 2
Results of the relationship between modeled and field estimation of GPP.

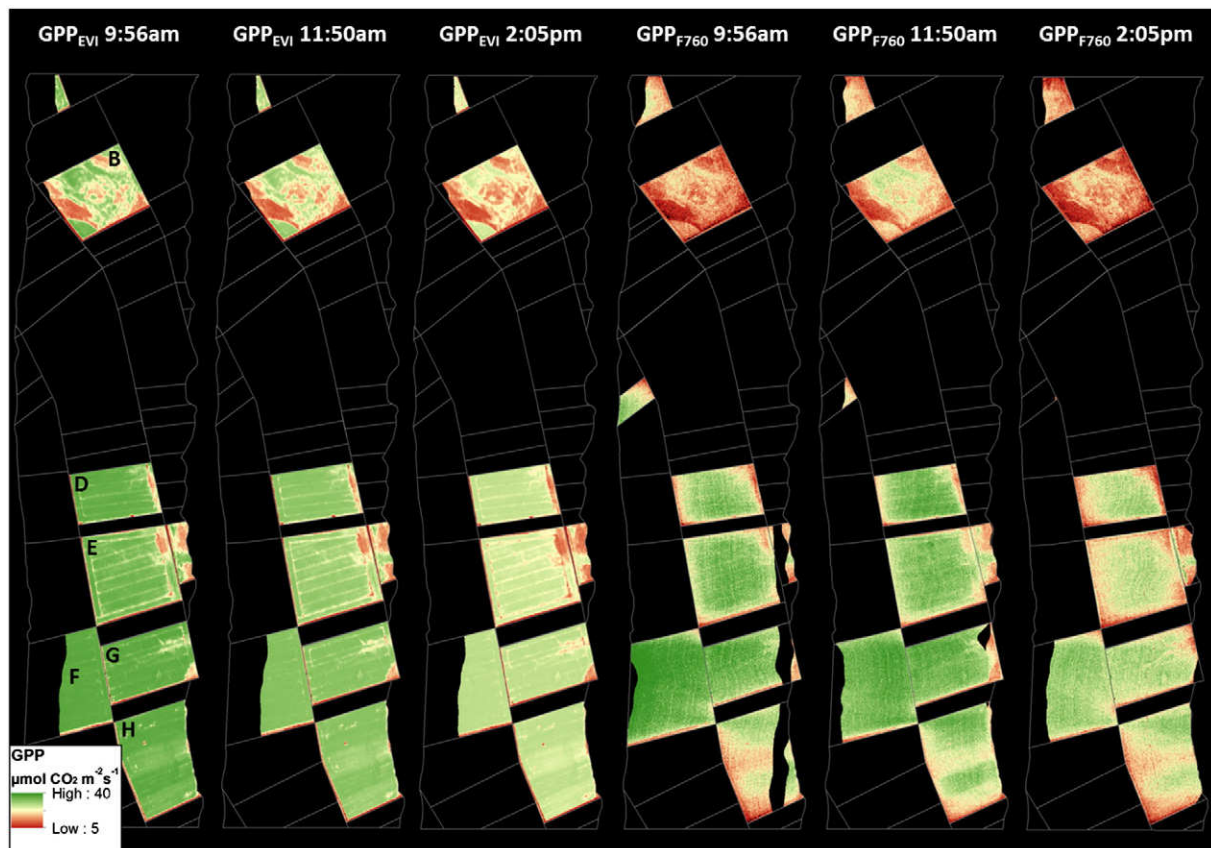|	LUE model (NDVI)	LUE model (EVI)	LUE model (MCARI2I)	LUE model (TCARI)	LUE model (PRI570)	F model
R^2	0.59	0.82	0.48	0.1	0.54	**0.87**
BIAS in %	−3.7	−3.7	1.33	7.44	−5.2	−5.88
Slope	0.32	0.48	0.28	0.17	0.3	**0.65**
RMSE	6.62	6.26	7.11	9.16	7.00	**4.34**
P-value	<0.05	<0.05	<0.05	0.16	<0.05	<0.05

Fig. 6. Scatter plot of GPPCC (estimated from ground based measurements, cf., Section 2.2.2) with GPPEVI (black x-marks, cf., Section 2.4.1) and with GPPF760 (yellow dots, cf., Section 0) and the corresponding linear regression fits. The blue line indicates the line of identity. Error bars indicate data uncertainty (cf., Section 2.5).

effects in combination with the illumination geometry rather than to plant adaptation to changing environmental conditions.

4.3. Sensitivity of fluorescence for plant functional changes

LUE_{CC} follows a typical diurnal cycle where values are highest early in the morning and decrease with excess light supply, high air temperatures and decreasing soil water contents due to high evapotranspiration (Hilker et al., 2008). Since the maximum air temperature during the observation period did not exceed 23 °C we assume that temperature alone is not a limiting factor. Further, the agricultural field was repeatedly fertilized, thus, nitrogen/nutrient deficits are unlikely. Therefore, we assume that the LUE was decreased by 1) a downregulation of photosynthesis due to high levels of incoming radiation and 2) the associated stomatal closure to reduce transpiration. The diurnal course of $F_{760yield,MSS}$ is similar to that of the LUE_{CC}, however, characterized by a different slope. During the decrease of LUE_{CC} and $F_{760yield,MSS}$, excess light energy is dissipated as heat (NPQ). The subsequent increase of LUE_{CC} and $F_{760yield,MSS}$ during the afternoon hours is most likely caused by a decrease of NPQ and a larger fraction of energy that is used for photosynthesis. These results indicate that in our study changing radiation conditions are, most likely, the dominant effect on the downregulation of photosynthesis during noon. The consistent use of F to estimate changes in photosynthetic activity critically relies on reliable estimates of NPQ. Several studies demonstrate the applicability of using PRI to estimate rates of NPQ in homogeneous canopies (Grace et al., 2007; Meroni et al., 2008; Rahimzadeh-Bajgiran et al., 2012; Weng et al., 2006). With the selection of FLEX as an Earth Explorer 8 mission, consistent global maps of F and NPQ (using PRI or more sophisticated canopy PRI derivatives, e.g. Hernández-Clemente et al. (2011)) will be available in the future. Future modeling studies should, hence,

effects and to soil reflectance (Huete et al., 2002), it estimated the upper and lower levels of plant productivity better than the other indices tested. However, the estimates of GPP$_{EVI}$ show both, saturation effects at a high canopy density and the effects of soil reflectance for sparse canopies. Since the EVI is particularly sensitive to canopy structure, fAPAR values did not change significantly across the investigated fields over the day. Minor changes are most likely related to surface anisotropy
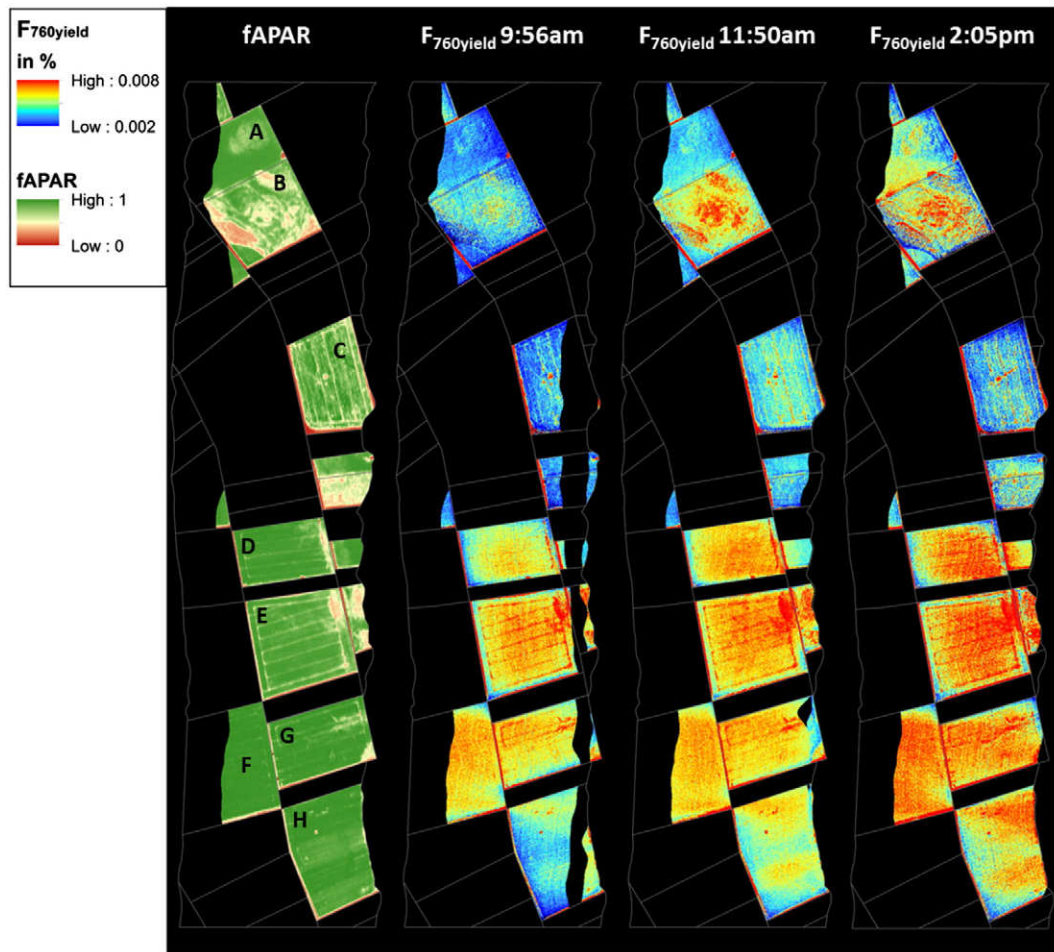

Fig. 7. Maps of estimated GPP for sugar beet based on EVI and F_{760} at 9:56 a.m., 11:50 a.m. and 2:05 p.m. UTC.

Fig. 8. Comparison of the spatial patterns effecting model driver. The maps are, from left to right, fAPAR estimated by EVI; F760yield at 9:56 a.m.; 11:50 a.m.; 2:05 p.m. UTC.

increase capability to consider the use of NPQ information as an additional input parameter to constrain RS-based estimates of GPP.

The highly variable ratio of LUE_{CC} to $F_{760yield,MSS}$ over the day, especially during early morning, (cf., Fig. 4D) contrast with the assumption of a constant ratio under moderate light conditions in the morning (Yoshida et al., 2015). Fig. 5 indicates a changing relationship of F_{yield} to LUE after solar noon. After solar noon, the LUE does not recover to the same level as before solar noon, which may be related to the still increasing temperature and progressive lower water availability. This finding suggests that diurnal LUE should not be easily linearly related to $F_{760yield}$.

The comparison of F maps in both peaks indicates that differences in canopy structure and species have an impact on F_{ratio} (cf. Fig. 2 & Fig. 3). During unstressed conditions, variations in F_{ratio} are most likely related to structural variables such as canopy chlorophyll content: F_{760} generally increases with increasing chlorophyll concentration while F_{687} decreases due to re-absorption of the emitted F signal in this wavelength (Buschmann, 2007). Under environmental stress (i.e., drought, heat), values of F_{ratio} can change due to changes in the leaf and canopy structure (e.g., leaf angle adjustments and movement (Arena et al., 2008; Kadioglu et al., 2012)), again affecting the re-absorption of red fluorescence. Moreover, these variations may be related to physiological changes that in turn affect F_{ratio}, which reflects a changing contribution of fluorescence emission from Photosystem I (PSI) and Photosystem II (PsiI) in response to plant stress (Porcar-Castell et al., 2014). A recent meta-analysis by Ač et al. (2015) showed that water-, temperature- and nitrogen-stress differ in their effect on F_{ratio}. Since rapeseed is still in the growing phase, high values of F_{ratio} are most likely linked to lower reabsorption due to low chlorophyll content and low leaf area.

High values of F_{ratio} in sugar beet fields with low EVI, however, cannot be solely linked to lower re-absorption effects. From electrical conductivity measurements and soil profiles it is known that various fields in this area show high gravel content, originating from sediments of a fossil river bed of the Rur river (Rudolph et al., 2015; Weihermüller et al., 2007). The high gravel content strongly affects the water holding capacity as well as the soil organic carbon. This results in a significant lower plant density in sugar beet field B and the eastern border of field D, E and G. With increasing temperature and low water availability, sugar beet plants located on the fossil river bed are strongly affected by water stress, compared to other plants. The derived F_{ratio} map captures this effect and reveals higher F_{ratio} values for water stressed plants, being in agreement with results discussed in Ač et al. (2015). Being able to track the variation of this ratio from unstressed to stressed conditions over time and space can therefore help in distinguishing between different sources of stress.

Maps of $F_{760yield}$ are characterized by a strong diurnal variability, which can be related to dynamic plant adaptation strategies to variable environmental conditions We showed that under non- and low stress conditions in the morning, the LUE presents an exponential decrease relative to $F_{760yield}$ (c.f. Fig. 5). After noon, this relationship becomes linear and $F_{760yield}$ increases much more strongly than LUE. A similar behavior can be observed in the *HyPlant* derived $F_{760yield}$ maps, where most fields present little changes in $F_{760yield}$ before noon and a stronger increase after noon. Interestingly, in sugar beet fields with high F_{ratio}, the $F_{760yield}$ is mostly constant over the day. We therefore assume that the positive relationship of LUE to F_{yield} could invert during strong environmental stress conditions, when NPQ reaches high levels (Fig. 8: Comparison of the spatial patterns effecting model driver. The maps are, from
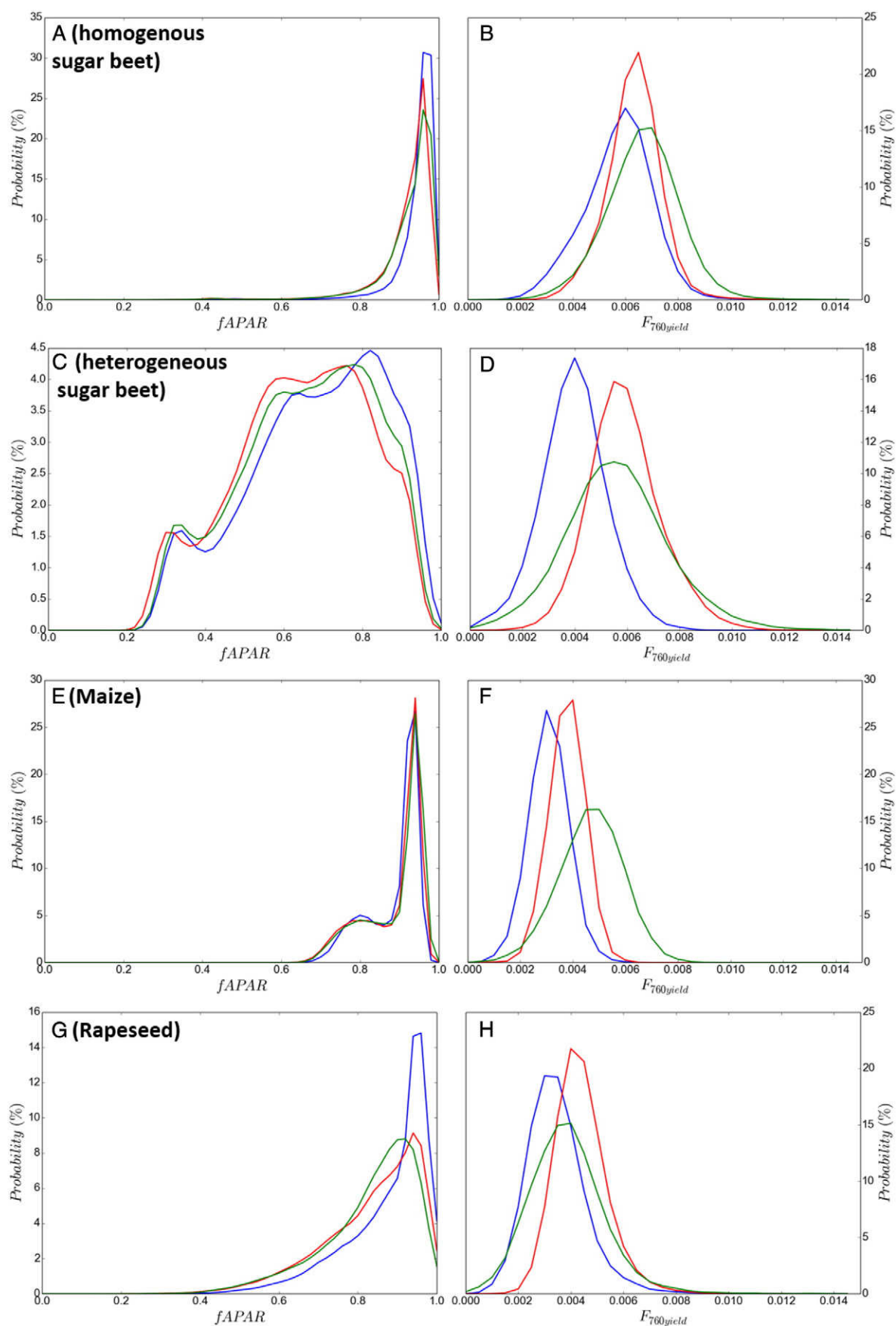
Fig. 9. Probability density function of fAPAR (left) and $F_{760yield}$ (right) for the overflights at 9:56 a.m. (blue), 11:50 a.m. (red) and 2:05 p.m. (green). Figs. A and B show the probability distribution of sugar beet fields D-H. Figs. C and D show the probability distribution of sugar beet fields B. Figs. E and F show the probability distribution of maize field A. Figs. G and H show the probability distribution of rapeseed field C.

left to right, fAPAR estimated by EVI; F760yield at 9:56 a.m.; 11:50 a.m.; 2:05 p.m. UTCFig. 8).

The different behavior in $F_{760yield}$ of sugar beet (low increase until noon and a subsequent stronger increase) compared to maize (steady but low increase over the day) might be explained by a better adaptation of C4 plants to dry and high light conditions, while the low $F_{760yield}$ in rapeseed could be associated to their early growing stage.

4.4. Reliability and transferability of the proposed GPP modeling approach

The correlation of GPP$_{EVI}$ and GPP$_{F760}$ with GPP$_{CC}$ (Fig. 6) indicates a better performance of the F-based estimation of GPP at low CO$_2$ assimilation rates. A potential explanation is that F$_{760}$ is not affected by signal contributions from the canopy background (e.g., soil, non-photosynthetic material). Still, the uncertainty levels of estimated GPP$_{F760}$ values highlight the need for improved instrumentation, particularly in terms of signal stability (SNR). Nevertheless, similar spatial patterns found for GPP$_{F760}$ and GPP$_{EVI}$ maps provide evidence that airborne-based F$_{760}$ measurements are sensitive to spatial variations of photosynthetic activity. The low GPP estimates from both models in field B; the eastern border of field D, E and the lower eastern corner of field G (Fig. 7), can be related to a high gravel content of the soils, originating from sediments of a fossil river bed of the Rur river (Rudolph et al., 2015; Weihermüller et al., 2007). The lower water holding capacity of such soils limits plant growth, which is clearly reflected in our observations.

5. Conclusions

Our results contribute to the previously published evidence that F facilitates improved estimates of GPP and its dynamics under changing environmental conditions. Due to the direct link between fluorescence and photosynthesis, complementary information compared to commonly used greenness based remote sensing variables can be retrieved from spectroscopic measurements. The significant lower values of F$_{760yield}$ in corn and rapeseed, the fundamentally different behavior of F$_{760yield}$ in sugar beet and maize during the day, and the changing F$_{687}$/F$_{760}$ relationship in time and across species are strong indicators of a distinct response of plant species to environmental stress and their F emission. Spatio-temporal patterns of combined F$_{687}$ and F$_{760}$ estimates and their relationship to APAR significantly contributes to our understanding of canopy structural effects on the re-absorption of F and of the delicate balance between the three competing pathways of photosynthesis, NPQ, and F. We conclude that plant photosynthesis, and thus GPP, is much more sensitive to environmental conditions in time and space than is considered in current modeling and observational approaches. The recently selected FLEX mission of ESA will provide all relevant parameters identified in this study (F in both peaks and PRI as a proxy for NPQ). Such information in combination with additional ground measurements yields a high potential to advance our understanding and capability to quantify biosphere dynamics in times of global change.

Acknowledgements

References

Ač, A., Malenovský, Z., Olejníčková, J., Gallé, A., Rascher, U., Mohammed, G., 2015. Meta-analysis assessing potential of steady-state chlorophyll fluorescence for remote sensing detection of plant water, temperature and nitrogen stress. Remote Sens. Environ. 168, 420–436. http://dx.doi.org/10.1016/j.rse.2015.07.022.

Alonso, L., Gomez-Chova, L., Vila-Frances, J., Amoros-Lopez, J., Guanter, L., Calpe, J., Moreno, J., 2008. Improved Fraunhofer line discrimination method for vegetation fluorescence quantification. IEEE Geosci. Remote Sens. Lett. 5, 620–624. http://dx.doi.org/10.1109/LGRS.2008.2001180.

Arena, C., Vitale, L., Santo, A.V.D., 2008. Paraheliotropism in Robinia pseudoacacia plants: an efficient means to cope with photoinhibition. In: Allen, J.F., Gantt, E., Golbeck, J.H., Osmond, B. (Eds.), Photosynthesis. Energy from the Sun. Springer, Netherlands, pp. 1403–1406.

Berk, A., Anderson, G.P., Acharya, P.K., Bernstein, L.S., Muratov, L., Lee, J., Fox, M.J., Adler-Golden, S.M., Chetwynd, J.H., Hoke, M.L., Lockwood, R.B., Cooley, T.W., Gardner, J.A., 2005. MODTRAN5: A Reformulated Atmospheric Band Model With Auxiliary Species and Practical Multiple Scattering Options. pp. 88–95 http://dx.doi.org/10.1117/12.578758.

Burkart, A., Schickling, A., Mateo, M.P.C., Wrobel, T.J., Rossini, M., Cogliati, S., Julitta, T., Rascher, U., 2015. A method for uncertainty assessment of passive sun-induced chlorophyll fluorescence retrieval using an infrared reference light. IEEE Sensors J. 15, 4603–4611. http://dx.doi.org/10.1109/JSEN.2015.2422894.

Buschmann, C., 2007. Variability and application of the chlorophyll fluorescence emission ratio red/far-red of leaves. Photosynth. Res. 92, 261–271. http://dx.doi.org/10.1007/s11120-007-9187-8.

Cogliati, S., Rossini, M., Julitta, T., Meroni, M., Schickling, A., Burkart, A., Pinto, F., Rascher, U., Colombo, R., 2015. Continuous and long-term measurements of reflectance and sun-induced chlorophyll fluorescence by using novel automated field spectroscopy systems. Remote Sens. Environ. 164, 270–281. http://dx.doi.org/10.1016/j.rse.2015.03.027.

Damm, A., Elbers, J., Erler, A., Gioli, B., Hamdi, K., Hutjes, R., Kosvancova, M., Meroni, M., Miglietta, F., Moersch, A., Moreno, J., Schickling, A., Sonnenschein, R., Udelhoven, T., van der Linden, S., Hostert, P., Rascher, U., 2010a. Remote sensing of sun-induced fluorescence to improve modeling of diurnal courses of gross primary production (GPP). Glob. Chang. Biol. 16, 171–186. http://dx.doi.org/10.1111/j.1365-2486.2009.01908.x.

Damm, A., Schickling, A., Schläpfer, D., Schaepman, M.E., Rascher, U., 2010b. Deriving sun-induced chlorophyll fluorescence from airborne based spectrometer data. ESA. http://dx.doi.org/10.5167/uzh-35343.

Damm, A., Erler, A., Hillen, W., Meroni, M., Schaepman, M.E., Verhoef, W., Rascher, U., 2011. Modeling the impact of spectral sensor configurations on the FLD retrieval accuracy of sun-induced chlorophyll fluorescence. Remote Sens. Environ. 115, 1882–1892. http://dx.doi.org/10.1016/j.rse.2011.03.011.

Damm, A., Guanter, L., Laurent, V.C.E., Schaepman, M.E., Schickling, A., Rascher, U., 2014. FLD-based retrieval of sun-induced chlorophyll fluorescence from medium spectral resolution airborne spectroscopy data. Remote Sens. Environ. 147, 256–266. http://dx.doi.org/10.1016/j.rse.2014.03.009.

Damm, A., Guanter, L., Paul-Limoges, E., van der Tol, C., Hueni, A., Buchmann, N., Eugster, W., Ammann, C., Schaepman, M.E., 2015. Far-red sun-induced chlorophyll fluorescence shows ecosystem-specific relationships to gross primary production: an assessment based on observational and modeling approaches. Remote Sens. Environ. 166, 91–105. http://dx.doi.org/10.1016/j.rse.2015.06.004.

Drolet, G.G., Middleton, E.M., Huemmrich, K.F., Hall, F.G., Amiro, B.D., Barr, A.G., Black, T.A., McCaughey, J.H., Margolis, H.A., 2008. Regional mapping of gross light-use efficiency using MODIS spectral indices. Remote Sens. Environ. 112, 3064–3078. http://dx.doi.org/10.1016/j.rse.2008.03.002.

Farquhar, G.D., von Caemmerer, S., Berry, J.A., 2001. Models of photosynthesis. Plant Physiol. 125, 42–45. http://dx.doi.org/10.1104/pp.125.1.42.

Field, C.B., Randerson, J.T., Malmström, C.M., 1995. Global net primary production: combining ecology and remote sensing. Remote Sensing of Land Surface for Studies of Global Change. Remote Sens. Environ. 51, pp. 74–88. http://dx.doi.org/10.1016/0034-4257(94)00066-V.

Franck, F., Juneau, P., Popovic, R., 2002. Resolution of the photosystem I and photosystem II contributions to chlorophyll fluorescence of intact leaves at room temperature. Biochim. Biophys. Acta BBA - Bioenerg. 1556, 239–246. http://dx.doi.org/10.1016/S0005-2728(02)00366-3.

Frankenberg, C., Fisher, J.B., Worden, J., Badgley, G., Saatchi, S.S., Lee, J.-E., Toon, G.C., Butz, A., Jung, M., Kuze, A., Yokota, T., 2011a. New global observations of the terrestrial carbon cycle from GOSAT: patterns of plant fluorescence with gross primary productivity. Geophys. Res. Lett. 38, L17706. http://dx.doi.org/10.1029/2011GL048738.

Frankenberg, C., Butz, A., Toon, G.C., 2011b. Disentangling chlorophyll fluorescence from atmospheric scattering effects in O2 A-band spectra of reflected sun-light. Geophys. Res. Lett. 38, L03801. http://dx.doi.org/10.1029/2010GL045896.

Frankenberg, C., O'Dell, C., Guanter, L., McDuffie, J., 2012. Remote sensing of near-infrared chlorophyll fluorescence from space in scattering atmospheres: implications for its retrieval and interferences with atmospheric CO2 retrievals. Atmos Meas Tech 5, 2081–2094. http://dx.doi.org/10.5194/amt-5-2081-2012.

Frankenberg, C., O'Dell, C., Berry, J., Guanter, L., Joiner, J., Koehler, P., Pollock, R., Taylor, T.E., 2014. Prospects for chlorophyll fluorescence remote sensing from the orbiting carbon observatory-2. Remote Sens. Environ. 147, 1–12. http://dx.doi.org/10.1016/j.rse.2014.02.007.

Gamon, J.A., Peñuelas, J., Field, C.B., 1992. A narrow-waveband spectral index that tracks diurnal changes in photosynthetic efficiency. Remote Sens. Environ. 41, 35–44. http://dx.doi.org/10.1016/0034-4257(92)90059-S.

Grace, J., Nichol, C., Disney, M., Lewis, P., Quaife, T., Bowyer, P., 2007. Can we measure terrestrial photosynthesis from space directly, using spectral reflectance and fluorescence? Glob. Chang. Biol. 13, 1484–1497. http://dx.doi.org/10.1111/j.1365-2486.2007.01352.x.

Graf, A., Werner, J., Langensiepen, M., van de Boer, A., Schmidt, M., Kupisch, M., Vereecken, H., 2013. Validation of a minimum microclimate disturbance chamber for net ecosystem flux measurements. Agric. For. Meteorol. 174–175, 1–14. http://dx.doi.org/10.1016/j.agrformet.2013.02.001.

Guanter, L., Frankenberg, C., Dudhia, A., Lewis, P.E., Gómez-Dans, J., Kuze, A., Suto, H., Grainger, R.G., 2012. Retrieval and global assessment of terrestrial chlorophyll fluorescence from GOSAT space measurements. Remote Sens. Environ. 121, 236–251. http://dx.doi.org/10.1016/j.rse.2012.02.006.

Guanter, L., Zhang, Y., Jung, M., Joiner, J., Voigt, M., Berry, J.A., Frankenberg, C., Huete, A.R., Zarco-Tejada, P., Lee, J.-E., Moran, M.S., Ponce-Campos, G., Beer, C., Camps-Valls, G., Buchmann, N., Gianelle, D., Klumpp, K., Cescatti, A., Baker, J.M., Griffis, T.J., 2014. Global and time-resolved monitoring of crop photosynthesis with chlorophyll fluorescence. Proc. Natl. Acad. Sci. 111, E1327–E1333. http://dx.doi.org/10.1073/pnas.1320008111.

Haboudane, D., Miller, J.R., Tremblay, N., Zarco-Tejada, P.J., Dextraze, L., 2002. Integrated narrow-band vegetation indices for prediction of crop chlorophyll content for application to precision agriculture. Remote Sens. Environ. 81, 416–426. http://dx.doi.org/10.1016/S0034-4257(02)00018-4.

Haboudane, D., Miller, J.R., Pattey, E., Zarco-Tejada, P.J., Strachan, I.B., 2004. Hyperspectral vegetation indices and novel algorithms for predicting green LAI of crop canopies: modeling and validation in the context of precision agriculture. Remote Sens. Environ. 90, 337–352. http://dx.doi.org/10.1016/j.rse.2003.12.013.

Hernández-Clemente, R., Navarro-Cerrillo, R.M., Suárez, L., Morales, F., Zarco-Tejada, P.J., 2011. Assessing structural effects on PRI for stress detection in conifer forests. Remote Sens. Environ. 115, 2360–2375. http://dx.doi.org/10.1016/j.rse.2011.04.036.

Hilker, T., Coops, N.C., Wulder, M.A., Black, T.A., Guy, R.D., 2008. The use of remote sensing in light use efficiency based models of gross primary production: a review of current status and future requirements. BIOGEOCHEMISTRY OF FORESTED ECOSYSTEM — Selected Papers From BIOGEOMON, the 5th International Symposium on Ecosystem Behaviour, held at the University of California, Santa Cruz, on June 25–30, 2006. Sci. Total Environ. 404, pp. 411–423. http://dx.doi.org/10.1016/j.scitotenv.2007.11.007.

Huete, A., Didan, K., Miura, T., Rodriguez, E.P., Gao, X., Ferreira, L.G., 2002. Overview of the radiometric and biophysical performance of the MODIS vegetation indices. The Moderate Resolution Imaging Spectroradiometer (MODIS): A New Generation of Land Surface Monitoring. Remote Sens. Environ. 83, pp. 195–213. http://dx.doi.org/10.1016/S0034-4257(02)00096-2.

Joiner, J., Yoshida, Y., Vasilkov, A.P., Yoshida, Y., Corp, L.A., Middleton, E.M., 2011. First observations of global and seasonal terrestrial chlorophyll fluorescence from space. Biogeosciences 8, 637–651. http://dx.doi.org/10.5194/bg-8-637-2011.

Joiner, J., Yoshida, Y., Vasilkov, A.P., Middleton, E.M., Campbell, P.K.E., Yoshida, Y., Kuze, A., Corp, L.A., 2012. Filling-in of near-infrared solar lines by terrestrial fluorescence and other geophysical effects: simulations and space-based observations from SCIAMACHY and GOSAT. Atmos Meas Tech 5, 809–829. http://dx.doi.org/10.5194/amt-5-809-2012.

Joiner, J., Guanter, L., Lindstrot, R., Voigt, M., Vasilkov, A.P., Middleton, E.M., Huemmrich, K.F., Yoshida, Y., Frankenberg, C., 2013. Global monitoring of terrestrial chlorophyll fluorescence from moderate-spectral-resolution near-infrared satellite measurements: methodology, simulations, and application to GOME-2. Atmos. Meas. Tech. 6, 2803–2823. http://dx.doi.org/10.5194/amt-6-2803-2013.

Jung, M., Reichstein, M., Margolis, H.A., Cescatti, A., Richardson, A.D., Arain, M.A., Arneth, A., Bernhofer, C., Bonal, D., Chen, J., Gianelle, D., Gobron, N., Kiely, G., Kutsch, W., Lasslop, G., Law, B.E., Lindroth, A., Merbold, L., Montagnani, L., Moors, E.J., Papale, D., Sottocornola, M., Vaccari, F., Williams, C., 2011. Global patterns of land-atmosphere fluxes of carbon dioxide, latent heat, and sensible heat derived from eddy covariance, satellite, and meteorological observations. J. Geophys. Res.-Biogeosciences 116, G00J07. http://dx.doi.org/10.1029/2010jg001566.

Kadioglu, A., Terzi, R., Saruhan, N., Saglam, A., 2012. Current advances in the investigation of leaf rolling caused by biotic and abiotic stress factors. Abiotic Stress Tolerances. Plant Sci. 182, pp. 42–48. http://dx.doi.org/10.1016/j.plantsci.2011.01.013.

Langensiepen, M., Kupisch, M., van Wijk, M.T., Ewert, F., 2012. Analyzing transient closed chamber effects on canopy gas exchange for optimizing flux calculation timing. Agric. For. Meteorol. 164, 61–70. http://dx.doi.org/10.1016/j.agrformet.2012.05.006.

Lanuv, N.R.W., 2014. Klimaatlas NRW.

Meroni, M., Rossini, M., Picchi, V., Panigada, C., Cogliati, S., Nali, C., Colombo, R., 2008. Assessing steady-state fluorescence and PRI from hyperspectral proximal sensing as early indicators of plant stress: the case of ozone exposure. Sensors 8, 1740–1754. http://dx.doi.org/10.3390/s8031740.

Meroni, M., Rossini, M., Guanter, L., Alonso, L., Rascher, U., Colombo, R., Moreno, J., 2009. Remote sensing of solar-induced chlorophyll fluorescence: review of methods and applications. Remote Sens. Environ. 113, 2037–2051. http://dx.doi.org/10.1016/j.rse.2009.05.003.

Meroni, M., Busetto, L., Colombo, R., Guanter, L., Moreno, J., Verhoef, W., 2010. Performance of spectral fitting methods for vegetation fluorescence quantification. Remote Sens. Environ. 114, 363–374. http://dx.doi.org/10.1016/j.rse.2009.09.010.

Monteith, J.L., 1972. Solar radiation and productivity in tropical ecosystems. J. Appl. Ecol. 9, 747–766. http://dx.doi.org/10.2307/2401901.

Monteith, J.L., Moss, C.J., 1977. Climate and the efficiency of crop production in Britain. Philos. Trans. R. Soc. Lond. Ser. B Biol. Sci. 281, 277–294. http://dx.doi.org/10.2307/2417832 [and discussion].

Plascyk, J.A., Gabriel, F.C., 1975. The Fraunhofer line discriminator MKII-an airborne instrument for precise and standardized ecological luminescence measurement. IEEE Trans. Instrum. Meas. 24, 306–313. http://dx.doi.org/10.1109/TIM.1975.4314448.

Porcar-Castell, A., Tyystjärvi, E., Atherton, J., van der Tol, C., Flexas, J., Pfündel, E.E., Moreno, J., Frankenberg, C., Berry, J.A., 2014. Linking chlorophyll a fluorescence to photosynthesis for remote sensing applications: mechanisms and challenges. J. Exp. Bot. eru191 http://dx.doi.org/10.1093/jxb/eru191.

Rahimzadeh-Bajgiran, P., Munehiro, M., Omasa, K., 2012. Relationships between the photochemical reflectance index (PRI) and chlorophyll fluorescence parameters and plant pigment indices at different leaf growth stages. Photosynth. Res. 113, 261–271. http://dx.doi.org/10.1007/s11120-012-9747-4.

Rascher, U., Agati, G., Alonso, L., Cecchi, G., Champagne, S., Colombo, R., Damm, A., Daumard, F., de Miguel, E., Fernandez, G., Franch, B., Franke, J., Gerbig, C., Gioli, B., Gómez, J.A., Goulas, Y., Guanter, L., Gutiérrez-de-la-Cámara, Ó., Hamdi, K., Hostert, P., Jiménez, M., Kosvancova, M., Lognoli, D., Meroni, M., Miglietta, F., Moersch, A., Moreno, J., Moya, I., Neininger, B., Okujeni, A., Ounis, A., Palombi, L., Raimondi, V., Schickling, A., Sobrino, J.A., Stellmes, M., Toci, G., Toscano, P., Udelhoven, T., van der Linden, S., Zaldei, A., 2009. CEFLES2: the remote sensing component to quantify photosynthetic efficiency from the leaf to the region by measuring sun-induced fluorescence in the oxygen absorption bands. Biogeosciences 6, 1181–1198. http://dx.doi.org/10.5194/bg-6-1181-2009.

Rascher, U., Alonso, L., Burkart, A., Cilia, C., Cogliati, S., Colombo, R., Damm, A., Drusch, M., Guanter, L., Hanus, J., Hyvärinen, T., Julitta, T., Jussila, J., Kataja, K., Kokkalis, P., Kraft, S., Kraska, T., Matveeva, M., Moreno, J., Muller, O., Panigada, C., Pikl, M., Pinto, F., Prey, L., Pude, R., Rossini, M., Schickling, A., Schurr, U., Schüttemeyer, D., Verrelst, J., Zemek, F., 2015. Sun-induced fluorescence — a new probe of photosynthesis: first maps from the imaging spectrometer HyPlant. Glob. Chang. Biol. http://dx.doi.org/10.1111/gcb.13017.

Reichstein, M., Falge, E., Baldocchi, D., Papale, D., Aubinet, M., Berbigier, P., Bernhofer, C., Buchmann, N., Gilmanov, T., Granier, A., Grünwald, T., Havránková, K., Ilvesniemi, H., Janous, D., Knohl, A., Laurila, T., Lohila, A., Loustau, D., Matteucci, G., Meyers, T., Miglietta, F., Ourcival, J.-M., Pumpanen, J., Rambal, S., Rotenberg, E., Sanz, M., Tenhunen, J., Seufert, G., Vaccari, F., Vesala, T., Yakir, D., Valentini, R., 2005. On the separation of net ecosystem exchange into assimilation and ecosystem respiration: review and improved algorithm. Glob. Chang. Biol. 11, 1424–1439. http://dx.doi.org/10.1111/j.1365-2486.2005.001002.x.

Rossini, M., Meroni, M., Migliavacca, M., Manca, G., Cogliati, S., Busetto, L., Picchi, V., Cescatti, A., Seufert, G., Colombo, R., 2010. High resolution field spectroscopy measurements for estimating gross ecosystem production in a rice field. Agric. For. Meteorol. 150, 1283–1296. http://dx.doi.org/10.1016/j.agrformet.2010.05.011.

Rossini, M., Nedbal, L., Guanter, L., Ač, A., Alonso, L., Burkart, A., Cogliati, S., Colombo, R., Damm, A., Drusch, M., Hanus, J., Janoutova, R., Julitta, T., Kokkalis, P., Moreno, J., Novotny, J., Panigada, C., Pinto, F., Schickling, A., Schüttemeyer, D., Zemek, F., Rascher, U., 2015. Red and far red Sun-induced chlorophyll fluorescence as a measure of plant photosynthesis. Geophys. Res. Lett. 42, 2014GL062943. http://dx.doi.org/10.1002/2014GL062943.

Rouse Jr., J.W., Haas, R.H., Schell, J.A., Deering, D.W., 1973. Monitoring Vegetation Systems in the Great Plains with Erts. NASA Spec. Publ. 351, 309.

Rudolph, S., van der Kruk, J., von Hebel, C., Ali, M., Herbst, M., Montzka, C., Pätzold, S., Robinson, D.A., Vereecken, H., Weihermüller, L., 2015. Linking satellite derived LAI patterns with subsoil heterogeneity using large-scale ground-based electromagnetic induction measurements. Geoderma 241–242, 262–271. http://dx.doi.org/10.1016/j.geoderma.2014.11.015.

Running, S.W., Nemani, R.R., Heinsch, F.A., Zhao, M., Reeves, M., Hashimoto, H., 2004. A continuous satellite-derived measure of global terrestrial primary production. Bioscience 54, 547–560. http://dx.doi.org/10.1641/0006-3568(2004)054[0547:ACSMOG]2.0.CO;2.

Ryu, Y., Baldocchi, D.D., Kobayashi, H., van Ingen, C., Li, J., Black, T.A., Beringer, J., van Gorsel, E., Knohl, A., Law, B.E., Roupsard, O., 2011. Integration of MODIS land and atmosphere products with a coupled-process model to estimate gross primary productivity and evapotranspiration from 1 km to global scales. Glob. Biogeochem. Cycles 25, GB4017. http://dx.doi.org/10.1029/2011GB004053.

Schimel, D., Pavlick, R., Fisher, J.B., Asner, G.P., Saatchi, S., Townsend, P., Miller, C., Frankenberg, C., Hibbard, K., Cox, P., 2015. Observing terrestrial ecosystems and the carbon cycle from space. Glob. Chang. Biol. 21, 1762–1776. http://dx.doi.org/10.1111/gcb.12822.

Sitch, S., Smith, B., Prentice, I.C., Arneth, A., Bondeau, A., Cramer, W., Kaplan, J.O., Levis, S., Lucht, W., Sykes, M.T., Thonicke, K., Venevsky, S., 2003. Evaluation of ecosystem dynamics, plant geography and terrestrial carbon cycling in the LPJ dynamic global vegetation model. Glob. Chang. Biol. 9, 161–185. http://dx.doi.org/10.1046/j.1365-2486.2003.00569.x.

Stadler, A., Rudolph, S., Kupisch, M., Langensiepen, M., van der Kruk, J., Ewert, F., 2015. Quantifying the effects of soil variability on crop growth using apparent soil electrical conductivity measurements. Eur. J. Agron. 64, 8–20. http://dx.doi.org/10.1016/j.eja.2014.12.004.

Turner, D.P., Ritts, W.D., Cohen, W.B., Gower, S.T., Zhao, M., Running, S.W., Wofsy, S.C., Urbanski, S., Dunn, A.L., Munger, J.W., 2003. Scaling gross primary production (GPP)

over boreal and deciduous forest landscapes in support of MODIS GPP product validation. Remote Sens. Environ. 88, 256–270. http://dx.doi.org/10.1016/j.rse.2003.06.005.

van der Tol, C., Verhoef, W., Timmermans, J., Verhoef, A., Su, Z., 2009. An Integrated Model of Soil-Canopy Spectral Radiances, Photosynthesis, Fluorescence, Temperature and Energy Balance. Biogeosciences 6 (no. 12), 3109–3129. http://dx.doi.org/10.5194/bg-6-3109-2009 (Dezember 2009).

Verhoef, W., Bach, H., 2003. Simulation of hyperspectral and directional radiance images using coupled biophysical and atmospheric radiative transfer models. Remote Sens. Environ. 87, 23–41. http://dx.doi.org/10.1016/S0034-4257(03)00143-3.

Verhoef, W., Bach, H., 2007. Coupled soil–leaf-canopy and atmosphere radiative transfer modeling to simulate hyperspectral multi-angular surface reflectance and TOA radiance data. Remote Sens. Environ. 109, 166–182. http://dx.doi.org/10.1016/j.rse.2006.12.013.

Wang, K., Liu, C., Zheng, X., Pihlatie, M., Li, B., Haapanala, S., Vesala, T., Liu, H., Wang, Y., Liu, G., Hu, F., 2013. Comparison between eddy covariance and automatic chamber techniques for measuring net ecosystem exchange of carbon dioxide in cotton and wheat fields. Biogeosciences 10, 6865–6877. http://dx.doi.org/10.5194/bg-10-6865-2013.

Weihermüller, L., Huisman, J.A., Lambot, S., Herbst, M., Vereecken, H., 2007. Mapping the spatial variation of soil water content at the field scale with different ground penetrating radar techniques. J. Hydrol. 340, 205–216. http://dx.doi.org/10.1016/j.jhydrol.2007.04.013.

Weng, J., Chen, Y., Liao, T., 2006. Relationships between chlorophyll fluorescence parameters and photochemical reflectance index of tree species adapted to different temperature regimes. Funct. Plant Biol. 33, 241–246.

Xiao, X., Zhang, Q., Braswell, B., Urbanski, S., Boles, S., Wofsy, S., Moore III, B., Ojima, D., 2004. Modeling gross primary production of temperate deciduous broadleaf forest using satellite images and climate data. Remote Sens. Environ. 91, 256–270. http://dx.doi.org/10.1016/j.rse.2004.03.010.

Xiao, J., Zhuang, Q., Baldocchi, D.D., Law, B.E., Richardson, A.D., Chen, J., Oren, R., Starr, G., Noormets, A., Ma, S., Verma, S., Wharton, S., Wofsy, S.C., Bolstad, P.V., Burns, S.P., Cook, D.R., Curtis, P.S., Drake, B.G., Falk, M., Fischer, M.L., Foster, D.R., Gu, L., Hadley, J.L., Hollinger, D.Y., Katul, G.G., Litvak, M., Martin, T.A., Matamala, R., McNulty, S., Meyers, T.P., Monson, R.K., Munger, J.W., Oechel, W.C., U, K.T.P., Schmid, H.P., Scott, R.L., Sun, G., Suyker, A.E., Torn, M.S., 2008. Estimation of Net Ecosystem Carbon Exchange for the Conterminous United States by Combining MODIS and AmeriFlux Data. Pap. Nat. Resour.

Yang, X., Tang, J., Mustard, J.F., Lee, J.-E., Rossini, M., Joiner, J., Munger, J.W., Kornfeld, A., Richardson, A.D., 2015. Solar-induced chlorophyll fluorescence that correlates with canopy photosynthesis on diurnal and seasonal scales in a temperate deciduous forest. Geophys. Res. Lett. 42, 2015GL063201. http://dx.doi.org/10.1002/2015GL063201.

Yoshida, Y., Joiner, J., Tucker, C., Berry, J., Lee, J.-E., Walker, G., Reichle, R., Koster, R., Lyapustin, A., Wang, Y., 2015. The 2010 Russian drought impact on satellite measurements of solar-induced chlorophyll fluorescence: insights from modeling and comparisons with parameters derived from satellite reflectances. Remote Sens. Environ. 166, 163–177. http://dx.doi.org/10.1016/j.rse.2015.06.008.

Zarco-Tejada, P.J., Catalina, A., González, M.R., Martín, P., 2013. Relationships between net photosynthesis and steady-state chlorophyll fluorescence retrieved from airborne hyperspectral imagery. Remote Sens. Environ. 136, 247–258. http://dx.doi.org/10.1016/j.rse.2013.05.011.

Zhang, Y., Guanter, L., Berry, J.A., Joiner, J., van der Tol, C., Huete, A., Gitelson, A., Voigt, M., Köhler, P., 2014. Estimation of vegetation photosynthetic capacity from space-based measurements of chlorophyll fluorescence for terrestrial biosphere models. Glob. Chang. Biol. 20, 3727–3742. http://dx.doi.org/10.1111/gcb.12664.